High-energy electrons produced in subpicosecond laser-plasma interactions from subrelativistic laser intensities to relativistic intensities

Y. T. Li, J. Zhang,* Z. M. Sheng, and J. Zheng
Laboratory of Optical Physics, Institute of Physics, Chinese Academy of Sciences, Beijing 100080, People's Republic of China

Z. L. Chen, R. Kodama, T. Matsuoka, M. Tampo, K. A. Tanaka, T. Tsutsumi, and T. Yabuuchi
Institute of Laser Engineering, Osaka University, 2-6 Yamada-Oka, Suita Osaka 565-0871, Japan
(Received 20 October 2003; published 23 March 2004)

The characteristics of the forward hot electrons produced by subpicosecond laser-plasma interactions are studied for different laser polarizations at laser intensities from subrelativistic to relativistic. The peak of the hot electron beam produced by *p*-polarized laser beam shifts to the laser propagation direction from the target normal direction as the laser intensity reaches the relativistic. For *s*-polarized laser pulse, hot electrons are mainly directed to the laser axis direction. The temperature and the maximum energy of hot electrons are much higher than that expected by the empirical scaling law. The energy spectra of the hot electrons evolve to be a single-temperature structure at relativistic laser intensities from the two-temperature structure at subrelativistic intensities. For relativistic laser intensities, the forward hot electrons are less dependent on the laser polarization under the laser conditions. The existing of a preplasma formed by the laser amplified spontaneous emission pedestal plays an important role in the interaction. One-dimensional particle-in-cell simulations reproduce the most characteristics observed in the experiment.

DOI: 10.1103/PhysRevE.69.036405 PACS number(s): 52.38.Kd, 52.50.Jm

I. INTRODUCTION

Large numbers of energetic electrons are generated in high intensity laser-foil interactions, some of them eject backward into vacuum from the underdense plasma. The others transport forward through the overdense plasma region first, then through the cold target region, and finally they escape from the rear of the foil target. Several generation mechanisms and transportation processes of the hot electrons have been proposed. A key parameter is the classical normalized momentum of electrons quivering in the laser electric field $a_0 = eE/m_e\omega_0 c = 8.5\times 10^{-10} I\lambda^{1/2}$, where I is the laser intensity in W/cm^2, λ is the laser wavelength in μm, e is the electron charge, E is the magnitude of the laser field, m_e is the electron mass, ω_0 is the laser angular frequency, and c is the velocity of light. For a subrelativistic laser intensity of $I\lambda^2 < 1.37\times 10^{18}$ W/cm^2 ($a_0 < 1$), the potential generation processes such as resonance absorption and vacuum heating will accelerate electrons in the target normal direction. While for a relativistic laser intensity of $I\lambda^2 > 1.37\times 10^{18}$ W/cm^2 ($a_0 > 1$) $J\times B$ heating, wake field, etc., dominate. They will accelerate electrons in the longitudinal direction.

The forward hot electrons are of significance in the fast ignition [1], in which the hot electron beam is produced in the interaction of short laser pulses with a large scale plasma formed by the nanosecond laser pulses. When a large length preplasma is formed in high intensity laser-plasma interactions, stochastic heating [2] and various parametric instabilities may also accelerate electrons [3].

The characteristics of the forward hot electrons have been studied under different laser conditions in many laboratories [4,5]. However, the dependence of hot electrons on laser intensities that are changed from subrelativistic to relativistic has been seldom systemically investigated at a specified laser facility, especially when a large scale preplasma, which is the practical case in the fast ignition, presents before the main laser pulses arrive. In this paper we study the spatial distributions, energy spectra, and numbers of hot electrons in the subpicosecond laser-large scale preplasma interactions for both *p*-polarized and *s*-polarized laser pulses at laser intensities available from the subrelativistic to the relativistic. It is found that the properties of the forward hot electrons change greatly when the parameter a_0 is increased to be greater than 1 from subrelativistic laser intensity.

II. EXPERIMENT

The experiments were carried out using the GEKKO Module II laser facility at the Institute of Laser Engineering, Osaka University. The experimental setup is illustrated schematically in Fig. 1(a). A 0.6 ps, 1.053 μm linearly polarized laser pulse with an energy up to 10 J was focused by a f/3.8 off-axis parabolic mirror onto a 5 μm thick aluminum foil target. The focal spot size was monitored by an *x*-ray pinhole camera. Figure 1(b) shows an *x*-ray image of aluminum target taken by the pinhole camera for a *p*-polarized laser pulse with an incidence angle of 45°. The diameter of the focus was about 30 μm. The laser intensity on targets was adjustable between $(2-40)\times 10^{17}$ W/cm^2. The pulse pedestal is about 3×10^{-3} starting from 700 ps before the main laser peak. Therefore, the main laser beam interacted with a preplasma generated by the amplified spontaneous emission (ASE) pedestal. The incident angle was 45° for both *p*-polarized laser pulses and *s*-polarized laser pulses.

The spatial distribution of forward hot electrons was measured behind the target by LiF (Mg, Cu, P) thermolumines-

*Email address: jzhang@aphy.iphy.ac.cn

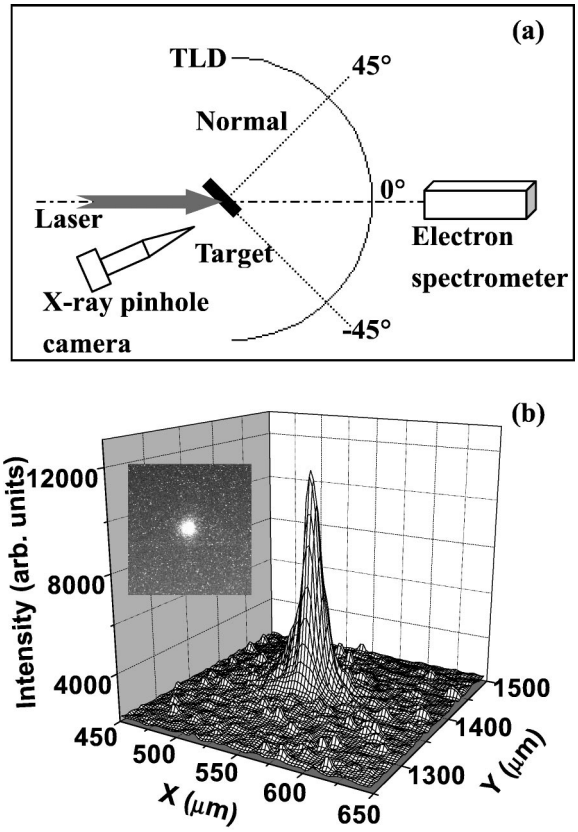

FIG. 1. (Color online) Schematic experimental setup. The spatial distribution of hot electrons ejected from the rear target surface were detected by TLDs behind the target. The energy distribution was measured by an electron spectrometer in the laser propagation direction. An x-ray pinhole camera was used to monitor the focal spot. the electron density of the preplasma was observed by a 2ω probe beam propagating perpendicular to the paper plane (not drawn). (b) An x-ray image and the intensity distribution of the laser focus measured by the pinhole camera.

cence dosimeters (TLDs) [6]. The dimension of the LiF detector is $\phi 4.5\times 0.75$ mm^2. The space behind the target was covered by more than one hundred TLDs mounted on a 2π spherical shell or a spherical ring. The distance from the focus to the TLD detectors was 45 mm. The angular resolution of the system was about 6°. The electron energy range was chosen by a composite filter in front of the detectors. The filter assembly consisted of aluminum filters with different thicknesses and a 200 μm thick radiochromic film. For some shots a piece of 1 mm thick CR39 was added as an ion detector in front of the filters.

An electron spectrometer with 2500 G permanent magnets was aligned in the laser propagation direction to measure the electron energy distribution. The acceptance angle of the spectrometer was 10^{-5} rad. The electron energy spectrum was recorded by calibrated imaging plates [7].

The electron density of the preplasma produced by the laser ASE pedestal preceding the main pulse were measured by optical interferometry. A small portion of the laser beam split from the main oscillator, after being amplified, compressed, and frequency-doubled to 527 nm, was used as a probe. The plasma was imaged on a 16 bit, 1018×1000 pixels charge-coupled device camera with a $10\times$ magnification. The acceptance angle of the optical system is about 0.1 rad. The interferograms were achieved by splitting the probe beam into two beams using a prism with an angle of 174°. An assembly of neutral filters and interference filters with a narrow bandwidth singled out the 527 nm probe beam from the background emission. The spatial resolution was about 9 μm. The time resolution was about 20 ps determined by the duration of the probe beam.

III. RESULTS AND DISCUSSION

A. Spatial distribution of hot electrons

Figure 2(a) shows a typical spatial distribution of the hot electrons behind a 5 μm thick aluminum target illuminated by *p*-polarized laser pulse with an incidence angle of 45° at an intensity of 28×10^{17} W/cm^2. Laser is incident in the *z*-axis direction. To see the results more clearly, the projection of the spatial distribution on the *x*-*y* plane and the angular distribution in the polarization plane are shown in Figs. 2(b) and 2(c), respectively. 0° and 45° corresponded to the laser propagation direction and the target normal direction respectively. A composite filter consisting of 1 mm thick CR39, 200 μm thick radiochromic film (RCF), and 5 μm thick aluminum were used for this shot. The TLDs are sensitive to electrons, ions, and x-ray passing the filter assembly. The maximum proton energy was less than 7 MeV for the laser intensity used in the experiment [8]. The composite filter can block all ions with energies less than 11 MeV. Therefore ions produced in the interaction cannot reach the detectors. Our simulations using ITS 3.0 code (Integrated TIGER Series of Coupled Electron/Photon) [9] shows that the x-ray signals are also negligible. Thus the dosage recorded by the TLDs detector was mainly caused by the hot electrons with energies greater than 0.55 MeV. We can see most of the hot electrons emitted into an elliptic region, which is located very close to the laser propagation direction and the long axis of the ellipticity parallels with the laser polarization direction. The emission cone angle of the hot electrons in the laser polarization plane is about 38° of the full width at half maximum (FWHM) obtained by a Gaussian fit to the experimental data.

Figure 3(a) shows the angular distribution of hot electrons at different laser intensities from the subrelativistic to the relativistic for the *p*-polarized laser pulse. The shadowed data are the angular distribution for hot electrons emitted in front of the target (see Fig. 1). Figure 3(b) shows the dependence of the FWHM of the divergence angle and the position of the hot electron peak on the parameter a_0, assuming the distribution to be Gaussian. More hot electrons are produced as the laser intensity increases. For $a_0\sim 1$, the widths of the cone angle is larger than those at other intensities. This is reasonable based on the basic understanding of hot electron generation. For $a_0<1$ the main electron acceleration mechanisms are the resonance absorption or vacuum heating etc., while for $a_0>1$ the hot electrons are accelerated in the longitudinal direction by $J\times B$ heating mechanism, etc. However, for $a_0\sim 1$ these mechanisms will compete, so that a wider cone angle of hot electrons is presented. One can also

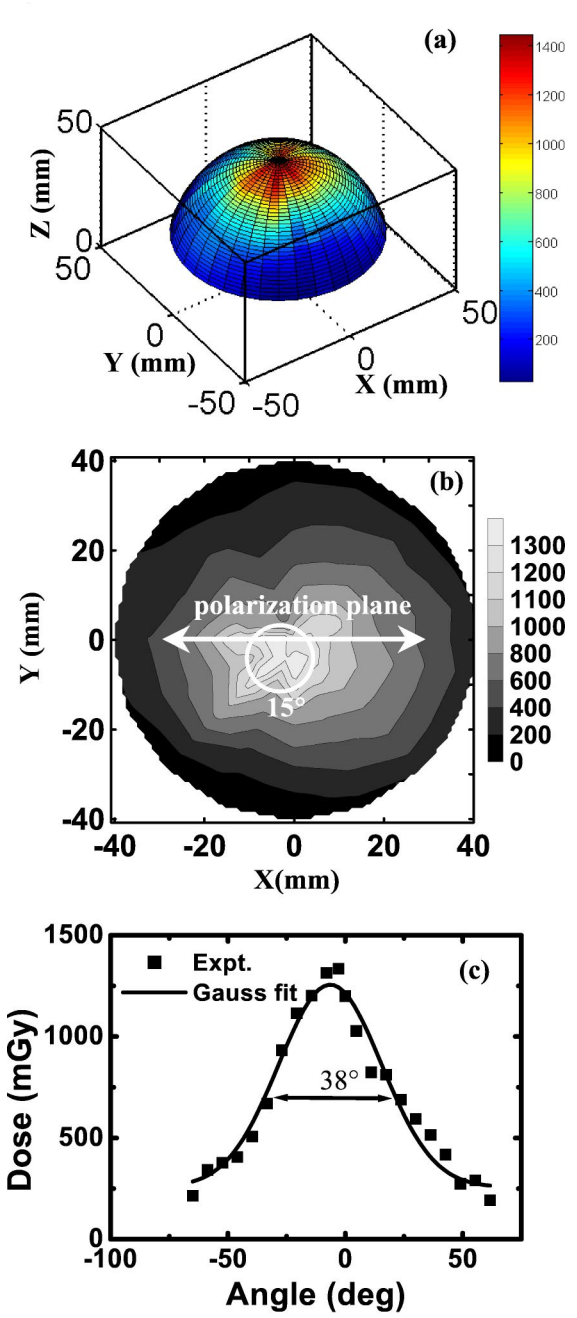

FIG. 2. (Color online) Typical spatial distribution of the hot electrons with energies greater than 0.55 MeV recorded by the TLDs behind the aluminum foil target for the *p*-polarized laser pulse at an intensity of 28×10^{17} W/cm^2 (a), the project on the *x*-*y* plane (b), and the angular distribution in the laser polarization plane (c).

see the position of the electron peak fall between the target normal and the laser axis when $a_0 \leqslant 1$. Only when the laser intensity is several times larger than the laser intensity of 1.37×10^{18} W/cm^2 ($a_0=1$) the hot electron beam turns to the laser propagation direction and the beam becomes well collimated.

Figure 4(a) shows the angular distributions of the hot electrons in the laser polarization plane for *s*-polarized laser

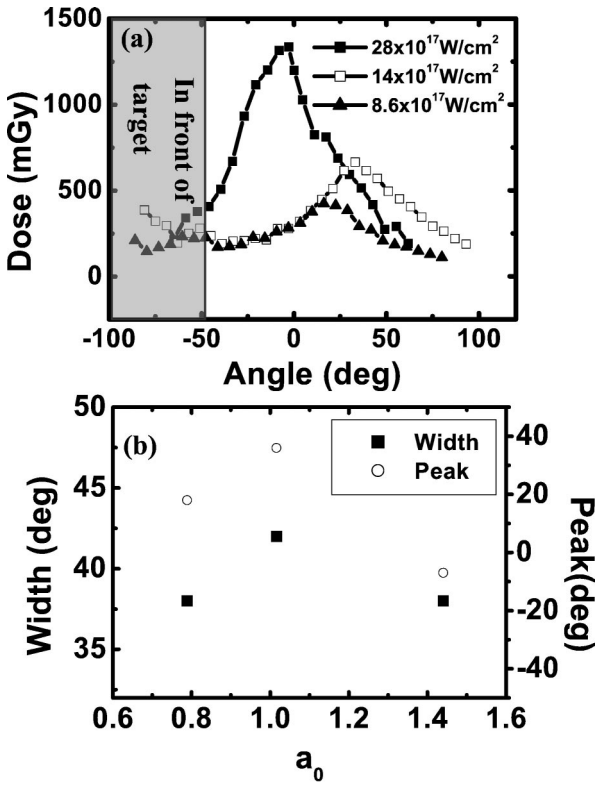

FIG. 3. (Color online) Angular distribution of the forward hot electrons produced by *p*-polarized laser pulse at three laser intensities (a). The shadowed data is the distribution in front of the target. (b) shows the dependence of the width of the emission cone angle and the peak position on the laser intensity.

beam. In order to compare the curves conveniently, the data values for the laser intensity of 40×10^{17} W/cm^2 were reduced by five times. The widths of the emission cone angles and the peak positions of the forward hot electrons are shown in Fig. 4(b). The electron beam is directed to the laser axis, with a maximum fluctuation of 10°. In our previous *s*-polarized femtosecond laser pulses-solid target experiments, for a_0 far less than 1 ($a_0\sim0.1$) it has been found that the two well-collimated hot electron beams are emitted in front of the target in the laser polarization direction due to the direct laser field acceleration [10]. When a_0 is between $\sim$0.5 and 1.2, the divergence angles of the hot electron beams in front of the target become wider and wider, and the peak positions move to the backward laser vector [11]. In this experiment we find that the hot electron emission behind the target shows similar trend. For $a_0 \leqslant 1$, the divergence angles increase with the laser intensity. However, when the laser intensity is several times larger than the laser intensity of 1.37×10^{18} W/cm^2 the hot electron beam becomes well collimated again. This indicates that the forward electron acceleration mechanisms dominate. Compared with the results of *p* polarization, one can see that the cone angle, the emission direction of the hot electrons for both *p* polarization and *s* polarization behave very similar when laser intensity is far larger than 1.37×10^{18} W/cm^2.

One can also see that the angular distributions are not smooth enough, in particular around the peak position. The

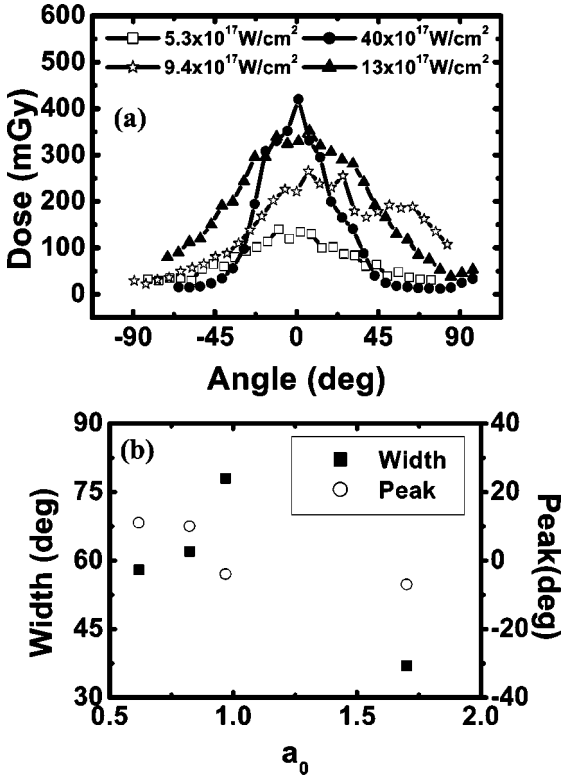

FIG. 4. (Color online). Angular distribution of the forward hot electrons produced by *s*-polarized laser pulse at four different laser intensities (a), the dependence of the width of the emission cone angle and the peak position on the laser intensity (b). The curve for the laser intensity of 40×10^{17} W/cm^2 is reduced by 5 times in order to compare the data clearly.

fine structure and the multiple small peaks may indicate the tearing processes of the hot electron beam and propagation instabilities in plasmas [12,13].

B. Energy distribution of hot electrons

Figures 5(a) and 5(b) show the energy spectra of the hot electrons ejected in the laser propagation for *p*-polarized laser pulse and *s*-polarized laser pulse at different laser intensities, respectively. The solid straight lines are the fitting curves using a Boltzmann distribution. We can see that for the subrelativistic laser intensity ($a_0<1$) two group hot electrons with different effect temperatures can be identified. However, as the laser intensity becomes relativistic ($a_0>1$), only one effect temperature presents for both the *p* polarization and the *s* polarization. This implies that the longitudinal acceleration mechanism gradually becomes dominant over other mechanisms as the laser intensity is increased to the relativistic.

Figure 5(c) shows the comparison of the energy spectra obtained at similar relativistic laser intensity for *p* polarization (32×10^{17} W/cm^2) and *s* polarization (28×10^{17} W/cm^2). The similarity of the energy spectra, emission directions, and the cone angles of the hot electrons measured for both polarizations indicate that the effects of the laser polarization on the forward hot electron generation is not as important in the relativistic laser plasma interactions as that in subrelativistic interactions [10].

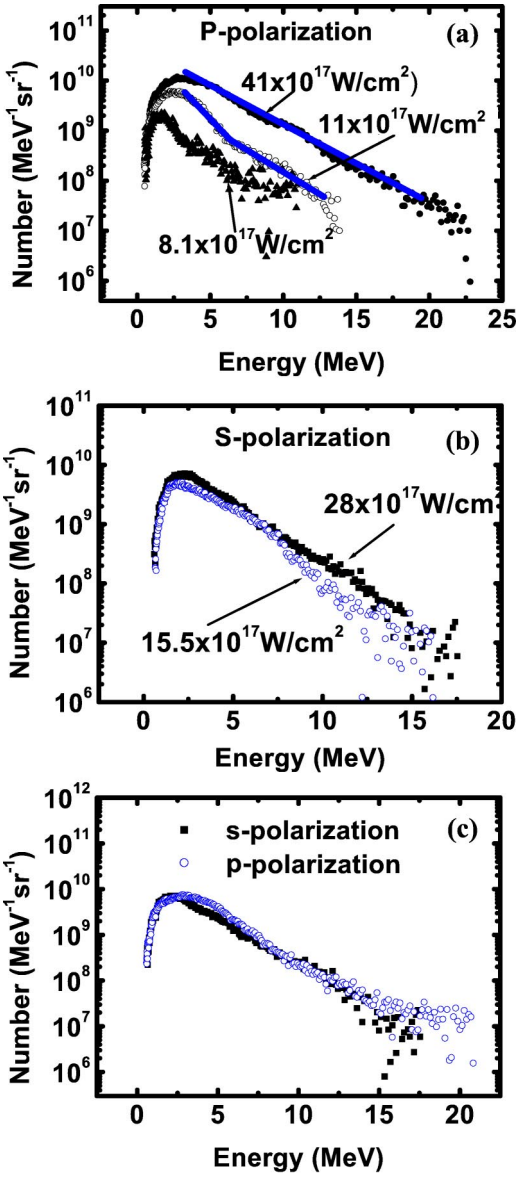

FIG. 5. (Color online). Energy distributions of the forward hot electrons exiting from the aluminum foil for *p*-polarized laser pulse (a), *s*-polarized laser pulse (b) at different laser intensities, and comparison of the energy distribution for *p* polarization at an intensity of 32×10^{17} W/cm^2 with that for *s*-polarization at an intensity of 28×10^{17} W/cm^2 (c). The solid lines are the exponential fit to the experimental data.

The measured energy of the hot electrons is significantly larger than that observed in previous experiments [4,14,15]. For example, for the *p*-polarized laser pulse at an intensity of 41×10^{17} W/cm^2 the effective temperature obtained by fitting an $\exp(-E/kT)$ to the tail of the energy distribution is about 3.0 MeV and the maximum energy is up to 20 MeV. As far as we know, this is the highest electron energy and temperature obtained in the subpicosecond laser-solid experiments at similar laser intensity. The energy and the temperature are much higher than that expected by the

ponderomotive potential scaling law, $kT=511[(1+I_{10^{18}\,\mathrm{Wcm}^{-2}}/1.37)^{1/2}-1]$ keV [16], and by the empirical scaling law proposed by Beg *et al.*, $kT=100(I_{10^{17}\mathrm{Wcm}^{-2}})^{1/3}$ keV [17]. A scaling relation of the hot electron temperature with laser intensity is usually obtained by fitting the experimental data measured under a specific laser and plasma condition, or is derived for a specific acceleration mechanism. Actually the hot electron energy depends not only on the laser intensity, but also on the electron density scale length of a preplasma, target material, laser duration, even on target thickness for forward electrons, etc. The hot electron generation mechanisms are also complicated and compete with each other. It is difficult for an empirical scaling law to take account of all these factors. Therefore it should be careful to use scaling laws to deduce the hot electron temperature for a specific experimental condition.

It is well known that the features of the hot electrons produced in the relativistic laser solid interactions are correlated with the plasma density scale length [18]. The contrast ratio of the laser beam in the experiments is $\sim 3\times 10^{-3}$. Consequently a preplasma will be formed before the main laser peak arrives. The spatial dimension of the preplasma can be modified by adjusting the ASE level. In the experiments we used interferometry to measure the electron density distribution of the preplasma. Figure 6(a) shows a typical interferogram of the preplasma formed by the ASE taken at 50 ps before the main beam. Figure 6(b) presents the effects of electron density scale length on the hot electron spectra produced by the *s*-polarized laser pulse at two similar laser intensities but with different contrast ratios, 16×10^{17} W/cm^2/3.8×10^{-3} (circled) and 15.5×10^{17} W/cm^2/2.4×10^{-3} (squared). The corresponding electron density distributions on the target normal for the two contrast ratios are shown in Fig. 6(c). The maximum electron energy and the distribution of the high-energy tail (>5 MeV) remain similar despite the difference of the preplasma. However, the numbers of the medium energy electrons (1–5 MeV) are enhanced greatly for the large electron density scale length.

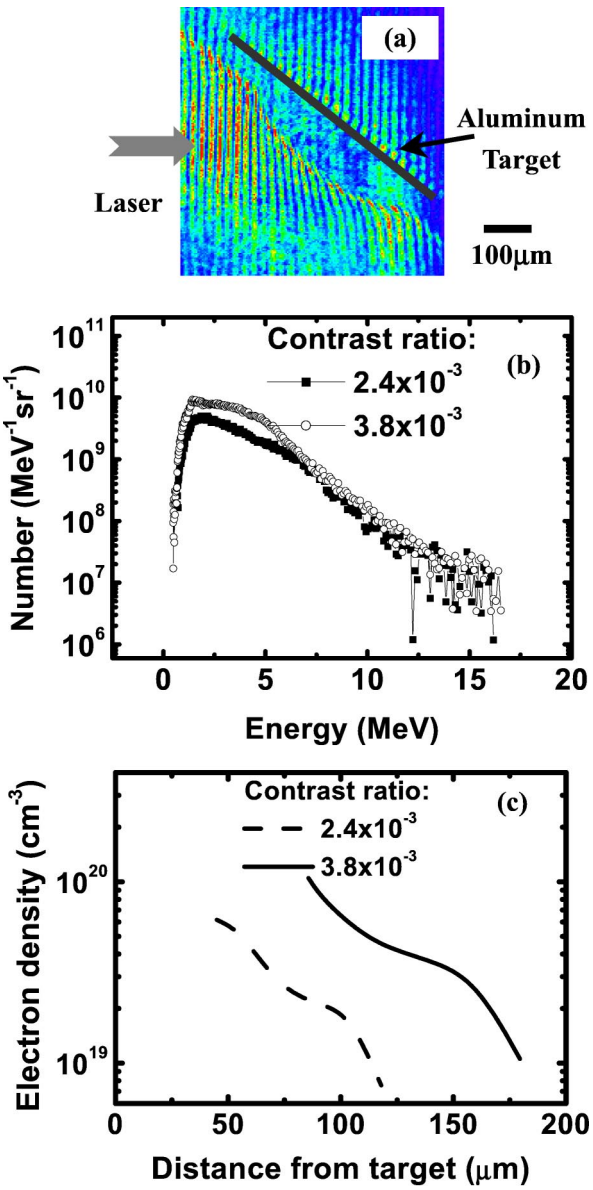

FIG. 6. (Color online). A typical interferogram of the preplasma taken at 50 ps before the main pulse (a), the energy spectra for two different ASE pedestals at the similar laser intensity of 16×10^{17} W/cm^2 (circle) and 15.5×10^{17} W/cm^2 (square) (b), and the corresponding electron density distributions of the preplasma (c). The *s*-polarized laser pulse is incident on a 5 μm aluminum foil at 45°.

C. Simulations

To understand the characteristics of the hot electrons generated under our experimental conditions, a one-dimensional fully relativistic particle-in-cell (PIC) code has been used to simulate the interaction of a high intensity laser pulse with a preplasma. The computation conditions are similar to the experimental parameters. The exponential electron density distributions shown in Fig. 7(a) is chosen based on the target thickness and the experimental measurements in Fig. 6(c). A 500 fs laser pulse is incident at 45° on such a preplasma with an intensity of 40×10^{17} W/cm^2. Both the electron spectrum obtained from the PIC simulation and the experimental spectrum for *p*-polarized laser pulse are plotted in Fig. 7(b). The simulation spectrum well reproduces the measurement spectrum for the hot electrons with higher energy (>2 MeV). The electrons can be accelerated to an energy over 20 MeV. The low-energy hot electron component measured by the spectrometer is affected by the charge separation field at the rear target surface seriously. The number of the low-energy hot electrons from the target will be reduced by the reflection and the recirculation movement of those electrons at the rear target surface [19]. However, the PIC simulation spectrum corresponds to the hot electron distribution inside the plasma. This can explain the discrepancy of the simulation and the measurement for the low-energy component.

Figure 7(c) shows the simulation spectra for *p*-polarized laser light and *s*-polarized laser light at the intensity of 40×10^{17} W/cm^2. The spectrum shapes are very similar to each other. This agrees with the experimental results shown in Fig. 5(c). The electron distribution in the momentum space $(\mathbf{P}_x,\mathbf{P}_y)$ plotted in Fig. 7(d) shows that the forward high-

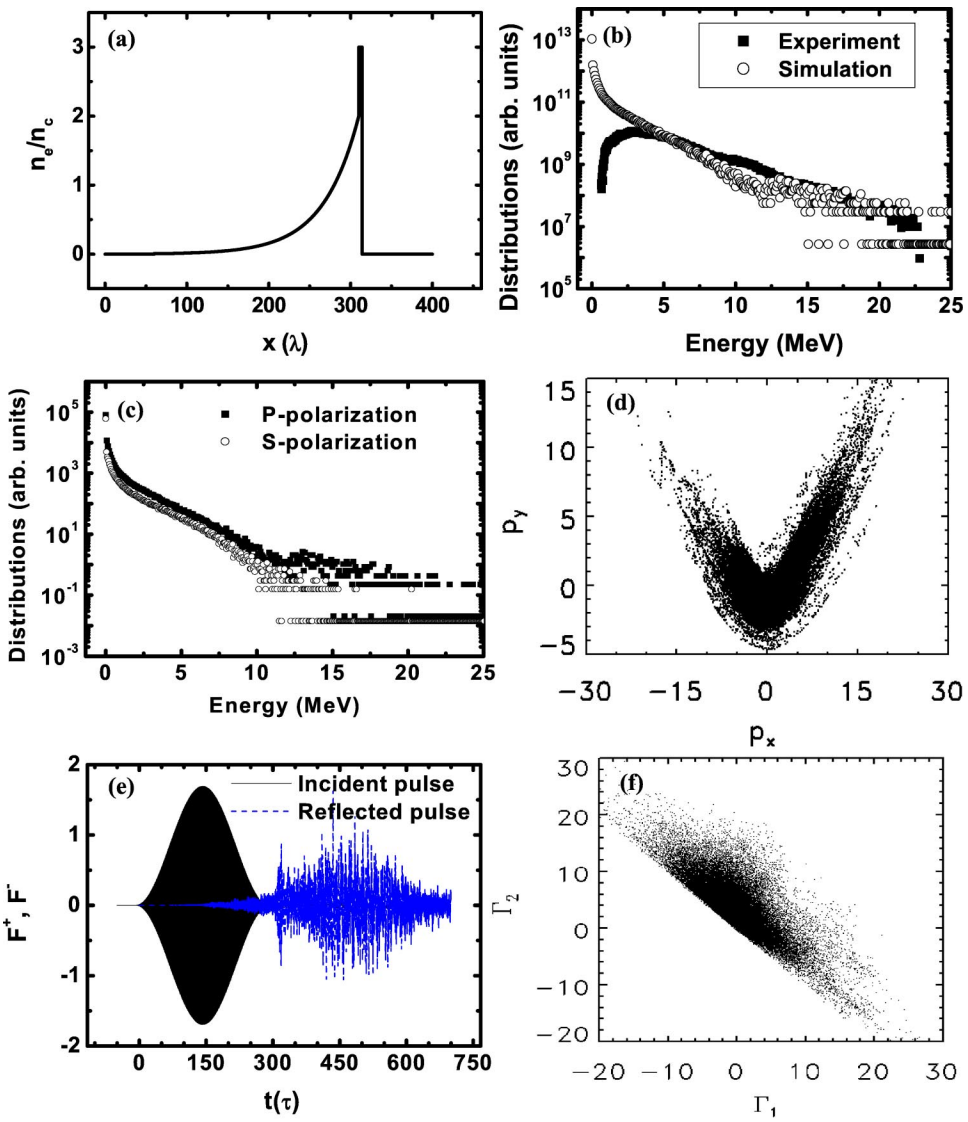

FIG. 7. (Color online). Results of the PIC simulation for *p*-polarized laser light. Laser is incident from the left at an intensity of 40 $\times 10^{17}$ W/cm^2. Initial electron density distribution of the preplasma (a), comparison of the simulation electron spectrum and the experimental spectrum (b), comparison of the simulation electron spectrum for the *p*-polarized light and *s*-polarized light (c), hot electron distribution in momentum space ($\mathbf{P}_x$,$\mathbf{P}_y$) (d), reflected light pulse from the preplasma (e), electron energy gain from longitudinal fields vs that from transverse laser fields (f).

energy electrons propagate in the laser axis direction mainly. The electron emission direction for *s*-polarization has also been simulated. It is found that the emission direction of the hot electron for *s*-polarized laser beam is the same as the case for *p*-polarization again. Both simulation and experiment show that the laser polarization has little effect on the electron energy distributions and emission direction at the relativistic laser intensity when a large scale preplasma presents. This is very much different from the interaction with short density gradient scale [16].

Except the well-known $J\times B$ heating mechanism, other hot electron generation mechanisms may also occur. In the experiments, the backward stimulated Brillouin scattering and the stimulated Raman scattering can occur in the large scale preplasma due to the laser ASE [20,21]. Our simulation shows that the integrated reflectivity of laser beam is as high as $\sim$20% at an intensity of 10^{18} W/cm^2 [see Fig. 7(e)]. The reflected light beams counterpropagate with the incident laser beam. This interaction configuration of two colliding laser pulses may accelerate electrons directly by the stochastic heating [2] or by the wake fields [22]. To clarify the electron energy gain from the transverse laser fields or from the longitudinal electric fields, the energy gain from transverse laser fields Γ_2 versus that from longitudinal fields in plasma Γ_1 is plotted in Fig. 7(f). One can see that the electrons are accelerated by both the longitudinal and the transverse fields together.

There are also some differences between PIC simulation and the measurement. The PIC simulations using two types of electron density distribution similar to that measured in Fig. 6(c) show that the hot electron spectra do not change as much as the experimental results. The simulations do not

reproduce the number increase of the hot electrons with medium energies measured in experiments shown in Fig. 6(b). The reasons are still not clear.

IV. SUMMARY

The characteristics of hot electrons produced by subpicosecond laser plasma interactions have been systemically studied for different laser polarizations at laser intensities transmitting from the subrelativistic to the relativistic. The laser conditions and the electron density distribution of the preplasma are fully monitored in the experiments. The peak of the hot electron beam produced by *p*-polarized laser beam moves expectedly to the laser propagation direction from the target normal direction as the laser intensity is increased to be relativistic. For *s*-polarized laser pulse, the hot electrons are directed to the laser axis direction mainly. The maximum energy of the hot electrons is accelerated to as high as 20 MeV and the average temperature of the hot electrons reaches up to 3.0 MeV at a laser intensity 41×10^{17} W/cm^2, which is much higher than that expected by the empirical scale law. The energy spectra of the hot electrons evolve to be a single-temperature structure at relativistic laser intensities from the two-temperature structure at subrelativistic intensities. For relativistic laser intensities, the angular distribution, energy spectra, and number of the forward hot electrons are less dependent on the laser polarization. The existence of a preplasma formed by the laser ASE pedestal plays an important role in the interaction. The electrons can gain energy both from the longitudinal laser fields and the transverse electric fields. One-dimensional PIC simulations reproduce many characteristics of the experimental measurement.

ACKNOWLEDGMENTS

We gratefully thank K. Sawai and K. Suzuki for operating the laser facility. This work was supported by the NNSFC (Project Nos. 10075075, 10105014, 10176034, 10374115), the National High-Tech ICF program, the NKBRSF (Grant No. G1999075206) and JSPS-CAS Core University Program on Plasma and Nuclear Fusion.

[1] M. Tabak *et al.*, Phys. Plasmas **1**, 1626 (1994).
[2] Z.-M. Sheng, K. Mima, Y. Sentoku, M.S. Jovanovic, T. Taguchi, J. Zhang, and J. Meyer-ter-Vehn, Phys. Rev. Lett. **88**, 055004 (2002).
[3] C. Rousseaux, M. Rabec le Gloahec, S.D. Baton, F. Amiranoff, J. Fuchs, L. Gremillet, J.C. Adam, A. Hron, and P. Mora, Phys. Plasmas **9**, 4261 (2002).
[4] G. Malka and J.L. Miquel, Phys. Rev. Lett. **77**, 75 (1996).
[5] R. Kodama *et al.*, Phys. Plasmas **8**, 2268 (2001).
[6] L.M. Chen, J. Zhang, H. Teng, Q.L. Dong, Z.L. Chen, T.J. Liang, L.Z. Zhao, and Z.Y. Wei, Phys. Rev. E **63**, 036403 (2001).
[7] T. Takahashi *et al.*, Ionizing Radiation **28**, 203 (2002) (in Japanese).
[8] E.L. Clark, K. Krushelnick, M. Zepf, F.N. Beg, M. Tatarakis, A. Machacek, M.I.K. Santala, I. Watts, P.A. Norreys, and A.E. Dangor, Phys. Rev. Lett. **85**, 1654 (2000).
[9] J.A. Halbleib *et al.*, ITS 3.0: Integrated TIGER Series of Coupled Electron/Photon Monte Carlo Transport Codes, SAND91-1634 (March 1992).
[10] L.M. Chen, J. Zhang, Y.T. Li, H. Teng, T.J. Liang, Z.M. Sheng, Q.L. Dong, L.Z. Zhao, Z.Y. Wei, and X.W. Tang, Phys. Rev. Lett. **87**, 225001 (2001).
[11] J. Zhang *et al.*, Phys. Rev. E (to be published).
[12] T. Taguchi, T.M. Antonsen, Jr., C.S. Liu, and K. Mima, Phys. Rev. Lett. **86**, 5055 (2001).
[13] M. Tatarakis, F.N. Beg, E.L. Clark, A.E. Dangor, R.D. Edwards, R.G. Evans, T.J. Goldsack, K.W.D. Ledingham, P.A. Norreys, M.A. Sinclair, M.-S. Wei, M. Zepf, and K. Krushelnick, Phys. Rev. Lett. **90**, 175001 (2003).
[14] K.B. Wharton, S.P. Hatchett, S.C. Wilks, M.H. Key, J.D. Moody, V. Yanovsky, A.A. Offenberger, B.A. Hammel, M.D. Perry, and C. Joshi, Phys. Rev. Lett. **81**, 822 (1998).
[15] U. Teubner, I. Uschmann, P. Gibbon, D. Altenbernd, E. Frster, T. Feurer, W. Theobald, R. Sauerbrey, G. Hirst, M.H. Key, J. Lister, and D. Neely, Phys. Rev. E **54**, 4167 (1996).
[16] S.C. Wilks, W.L. Kruer, M. Tabak, and A.B. Langdon, Phys. Rev. Lett. **69**, 1383 (1992).
[17] F.N. Beg *et al.*, Phys. Plasmas, **4**, 447 (1997).
[18] M.I.K. Santala, M. Zepf, I. Watts, F.N. Beg, E. Clark, M. Tatarakis, K. Krushelnick, A.E. Dangor, T. McCanny, I. Spencer, R.P. Singhal, K.W.D. Ledingham, S.C. Wilks, A.C. Machacek, J.S. Wark, R. Allott, R.J. Clarke, and P.A. Norreys, Phys. Rev. Lett. **84**, 1459 (2000).
[19] A.J. Mackinnon, Y. Sentoku, P.K. Patel, D.W. Price, S. Hatchett, M.H. Key, C. Andersen, R. Snavely, and R.R. Freeman, Phys. Rev. Lett. **88**, 215006 (2002).
[20] C. Rousseaux, M. Rabec le Gloahec, S.D. Baton, F. Amiranoff, J. Fuchs, L. Gremillet, J.C. Adam, A. Hron, and P. Mora, Phys. Plasmas **9**, 4261 (2002).
[21] C. Rousseaux, G. Malka, J.L. Miquel, F. Amiranoff, S.D. Baton, and Ph. Mounaix, Phys. Rev. Lett. **74**, 4655 (1995).
[22] G. Shvets, N.J. Fisch, A. Pukhov, and J. Meyer-ter-Vehn, Phys. Rev. E **60**, 2218 (1999).